Structural insights into ring-building motif domains involved in bacterial sporulation

Bowen Liu [a,1], Helena Chan [b,1], Elda Bauda [a], Carlos Contreras-Martel [a], Laure Bellard [a], Anne-Marie Villard [a], Caroline Mas [a], Emmanuelle Neumann [a], Daphna Fenel [a], Adrien Favier [a], Monica Serrano [c], Adriano O. Henriques [c], Christopher D.A. Rodrigues [b,*], Cecile Morlot [a,*]

[a] *Univ. Grenoble Alpes, CNRS, CEA, IBS, 38000 Grenoble, France*
[b] *The ithree institute, University of Technology Sydney, 2007 Ultimo, NSW, Australia*
[c] *Instituto de Tecnologia Quimica e Biologica, Universidade Nova de Lisboa, Oeiras, Portugal*

ARTICLE INFO

ABSTRACT

Components of specialized secretion systems, which span the inner and outer membranes in Gram-negative bacteria, include ring-forming proteins whose oligomerization was proposed to be promoted by domains called RBM for "Ring-Building Motifs". During spore formation in Gram-positive bacteria, a transport system called the SpoIIIA-SpoIIQ complex also assembles in the double membrane that surrounds the forespore following its endocytosis by the mother cell. The presence of RBM domains in some of the SpoIIIA proteins led to the hypothesis that they would assemble into rings connecting the two membranes and form a conduit between the mother cell and forespore. Among them, SpoIIIAG forms homo-oligomeric rings *in vitro* but the oligomerization of other RBM-containing SpoIIIA proteins, including SpoIIIAH, remains to be demonstrated. In this work, we identified RBM domains in the YhcN/YlaJ family of proteins that are not related to the SpoIIIA-SpoIIQ complex. We solved the crystal structure of YhcN from *Bacillus subtilis*, which confirmed the presence of a RBM fold, flanked by additional secondary structures. As the protein did not show any oligomerization ability *in vitro*, we investigated the structural determinants of ring formation in SpoIIIAG, SpoIIIAH and YhcN. We showed that *in vitro*, the conserved core of RBM domains alone is not sufficient for oligomerization while the β-barrel forming region in SpoIIIAG forms rings on its own. This work suggests that some RBMs might indeed participate in the assembly of homomeric rings but others might have evolved toward other functions.

1. Introduction

Specialized secretion systems found in Gram-negative bacteria allow the transport of molecules across their double-membrane cell envelope (Costa et al., 2015; Green and Mecsas, 2016). Components of these nanomachines include ring-forming proteins from the SctJ (PrgK) and SctD (PrgH) families, which are part of the inner membrane platform in Type-III secretion systems, and from the SctC (InvG) and GspD secretins from Type-III and Type-II secretion systems, respectively (Bergeron et al., 2015; Filloux and Voulhoux, 2018; Hu et al., 2018; Korotkov et al., 2011; Worrall et al., 2016; Yan et al., 2017). Homo-oligomerization of these proteins involves a family of domains called RBM for "Ring-Building Motif" (Spreter et al., 2009). These domains contain a core region displaying low sequence identity but a conserved wedge-shaped

fold composed of a three-stranded β-sheet packed against two α-helices. Two main secondary structure topologies have been observed so far: RBMs found in proteins of the inner membrane platform of T3SS display an αββαβ fold while RBMs found in outer membrane proteins (secretins) display a βαββα fold (Zeytuni et al., 2017). Finally, additional secondary structures can be present at the N-terminus or C-terminus, or inserted within the RBM core (Johnson et al., 2020; Levdikov et al., 2012; Meisner et al., 2012; Rodrigues et al., 2016; Trouve et al., 2018; Zeytuni et al., 2017).

Because the cell envelope of Gram-positive bacteria possess a single membrane, double-membrane spanning machineries are not necessary for secretion. During spore formation in Gram-positive bacteria however, the mother cell engulfs the developing spore, encasing it with a double membrane (Higgins and Dworkin, 2012; Tan and Ramamurthi,

---

2014). Communication between the two cells involves the assembly of a large multi-protein complex spanning the outer and inner forespore membranes, that may be involved in transporting metabolites or proteins, required for spore development (Morlot and Rodrigues, 2018; Riley et al., 2021). The architecture of this macromolecular machinery, called the SpoIIIA-SpoIIQ complex, remains mysterious but its components display structural similarities with essential constituents of specialized secretion systems (Camp and Losick, 2008; Meisner et al., 2008; Morlot and Rodrigues, 2018; Zeytuni and Strynadka, 2019). In particular, some of the SpoIIIA-SpoIIQ proteins possess RBM domains and one of them, called SpoIIIAG, forms large 30-mer rings that display remarkable similarities with SctJ, SctD and FliF rings from Type-III secretion systems (Bergeron et al., 2015; Johnson et al., 2020; Rodrigues et al., 2016; Zeytuni et al., 2017). Ring formation by SpoIIIAG provided structural evidence that the SpoIIIA-SpoIIQ complex serves as a transport machinery between the mother cell and forespore; however, assembly of a transenvelope channel requires oligomerization of other SpoIIIA-SpoIIQ proteins. Since SpoIIIAF, SpoIIIAH and GerM also possess RBM domains (Levdikov et al., 2012; Meisner et al., 2012; Trouve et al., 2018; Zeytuni et al., 2018), they represent obvious candidates for the formation of rings which would lean to that of SpoIIIAG. However so far, ring oligomerization of these proteins remains to be demonstrated.

Here, we discovered that four genes unrelated to the SpoIIIA-SpoIIQ complex also contain a putative RBM domain (Fig. S1). These genes, called *yutC*, *ylaJ*, *yhcN* and *coxA*, are transcribed during sporulation in *B. subtilis* and all have σG-dependent promoters, implying that their expression takes place in the forespore during late stages in the process (Eichenberger et al., 2004; Steil et al., 2005). In this study, we focused on the *yhcN* gene, which generates one of the most abundant mRNAs in spores (Korza et al., 2019). YhcN encodes a lipoprotein anchored in the spore inner membrane, but YhcN is also detected as a processed form (encompassing residues N40 to E189) in material released from germinating spores (Bagyan et al., 1998; Chirakkal et al., 2002; Kuwana et al., 2002; Zheng et al., 2016). The putative RBM domain in YhcN encompasses residues D78 to N150, and is located downstream of a region predicted to be unstructured (residues A24 to N77). Intriguingly, this N-terminal region displays a high level of asparagine, as observed in the small, acid-soluble spore proteins (SASPs), which contribute to DNA protection in dormant spores and are degraded upon spore germination to provide amino acids required for spore outgrowth (Setlow, 2006, 1995, 1988). The implication of this high content of asparagine residues in YhcN however remains mysterious so far. In the absence of YhcN, *B. subtilis* spores germinate slower than wild-type ones, due to impaired loss of heat resistance, slower DPA (dipicolinic acid) release and spore rehydration (Johnson and Moir, 2017). The later defect was shown to be related to SleB-associated cortex hydrolysis (Johnson and Moir, 2017). However, since YhcN inactivation also affects the loss of heat resistance and DPA release, this protein was proposed to play an additional role in earlier germination events. Altogether, these observations suggest that YhcN might have various roles in spore germination and outgrowth, and might be functionally linked to RBM-containing transport proteins, SASPs and/or cortex degrading enzymes.

In this study, we sought to provide further insights into the structure and function of YhcN's putative RBM domain. We provide data indicating that YhcN has only a minor role in spore germination, that appears to be independent of SleB. On the other hand, we solved its crystal structure, which confirmed the presence of a RBM domain. Like SpoIIIAH however, YhcN does not show any ability to oligomerize *in vitro*. To further determine the structural determinants of RBM domain oligomerization, we explored the capacity of different YhcN, SpoIIIAH and SpoIIIAG recombinant constructs to oligomerize. Our data suggest that the conserved core of RBM domains alone might not be sufficient to trigger oligomerization when proteins are isolated from their cellular context. By contrast, the β-triangle region inserted in the RBM core of SpoIIIAG can form rings on its own. Altogether, this work questions the ring-triggering function associated with RBM domains and suggests that some of these domains, including YhcN RBM, might have evolved to fulfill different roles.

2. Results and discussion

2.1. YhcN has a non-essential role in spore germination and outgrowth

A first attempt to identify functional homologues of YhcN using a standard protein blast search (https://blast.ncbi.nlm.nih.gov) was unsuccessful, indicating that YhcN does not display strong sequence identity with characterized protein domains. On the other hand, a search for remote protein homology using the HHpred server (https://toolkit. tuebingen.mpg.de) (Zimmermann et al., 2018) identified secondary structure similarity with the SctJ, SctD and FliF family of RBM-containing proteins involved in T3SS, suggesting that YhcN might be a ring-forming component of a new transport machinery.

As a first step in the characterization of YhcN, we investigated its cellular localization using a C-terminal mCherry fusion. YhcN-mCherry displayed a uniform membrane localization around the engulfed forespores from about 3 h after the onset of sporulation (Fig. 1A). In support of this observation, a similar localization pattern delineating the engulfed membrane was observed when YhcN was immunolabeled with anti-YhcN sera (Fig. 1B).

In order to carry out a structure–function study of YhcN, we sought to prepare ΔyhcN deletion strains that were previously reported to be affected in spore germination, outgrowth or colony-forming ability (Bagyan et al., 1998; Johnson and Moir, 2017). YhcN was previously shown to be linked to the cortex lytic activity of SleB, which becomes essential for cortex degradation upon inactivation of the CwlJ hydrolase (Ishikawa et al., 1998; Johnson and Moir, 2017). Recruitment and localization of a CwlJ-YFP fusion to the spore surface is SafA-dependent (McKenney and Eichenberger, 2012). CwlJ, however, is not detected in coat extracts prepared from a ΔcotE mutant strain (Amon et al., 2020). Possibly, and as described for inner coat proteins (Costa et al., 2004), recruitment of CwlJ to the surface of the developing spore might be SafA-dependent, but the protein does not persist in stable association with the spore when the outer coat fails to be formed, as in a ΔcotE mutant. In any event, in a ΔcotE mutant, the accumulation of CwlJ in the spore is diminished and the CwlJ-dependent hydrolysis of the cortex during germination is impaired (Amon et al., 2020; Bagyan and Setlow, 2002). We thus used a ΔcotE mutant, in which cortex hydrolysis was shown to require SleB and the presence of YhcN (Ishikawa et al., 1998; Johnson and Moir, 2017). We found that the colony-forming ability of ΔyhcN spores was 82% (±7%, n = 3) compared to wild-type, and that yhcN deletion did not show a strong cumulative effect on the colony-forming ability of ΔcotE spores (62% ± 6%, n = 3 for ΔcotE spores; 46% ± 3%, n = 3 for ΔcotE ΔyhcN spores) (Fig. 2A). Upon closer inspection of spore outgrowth, the yhcN deletion slowed down spore outgrowth by about 30 min when compared to the wild-type strain (Fig. 2C–D), in agreement with previous reports (Bagyan et al., 1998; Johnson and Moir, 2017). However, the absence of yhcN had little effect on the outgrowth of ΔcotE spores (Fig. 2C–D). Altogether, these experiments indicate that impairment of YhcN has only a mild effect on spore outgrowth and colony-forming ability, and that this effect is not strongly related to CotE-dependent processes, such as cortex degradation by SleB.

To exclude a potential role in sporulation that might have been missed previously, we analyzed key aspects of the sporulation cycle, including the activity of sigma factors, the assembly of the coat and heat resistance of the mature spores. Absence of YhcN neither affected the activation of sigma factors (Fig. S2) nor the localization of major coat proteins (SpoIVA, SpoVM, SafA, SpoVID and CotE) (Fig. S3). In heat-kill assays, ΔyhcN spores were only slightly affected compared to wild-type (97% ± 11%, n = 3, Fig. 2B), most likely due to their slight defect in colony-forming ability. Finally in the absence of CotE, deletion of yhcN only mildly reduced heat resistance, as the sporulation efficiency
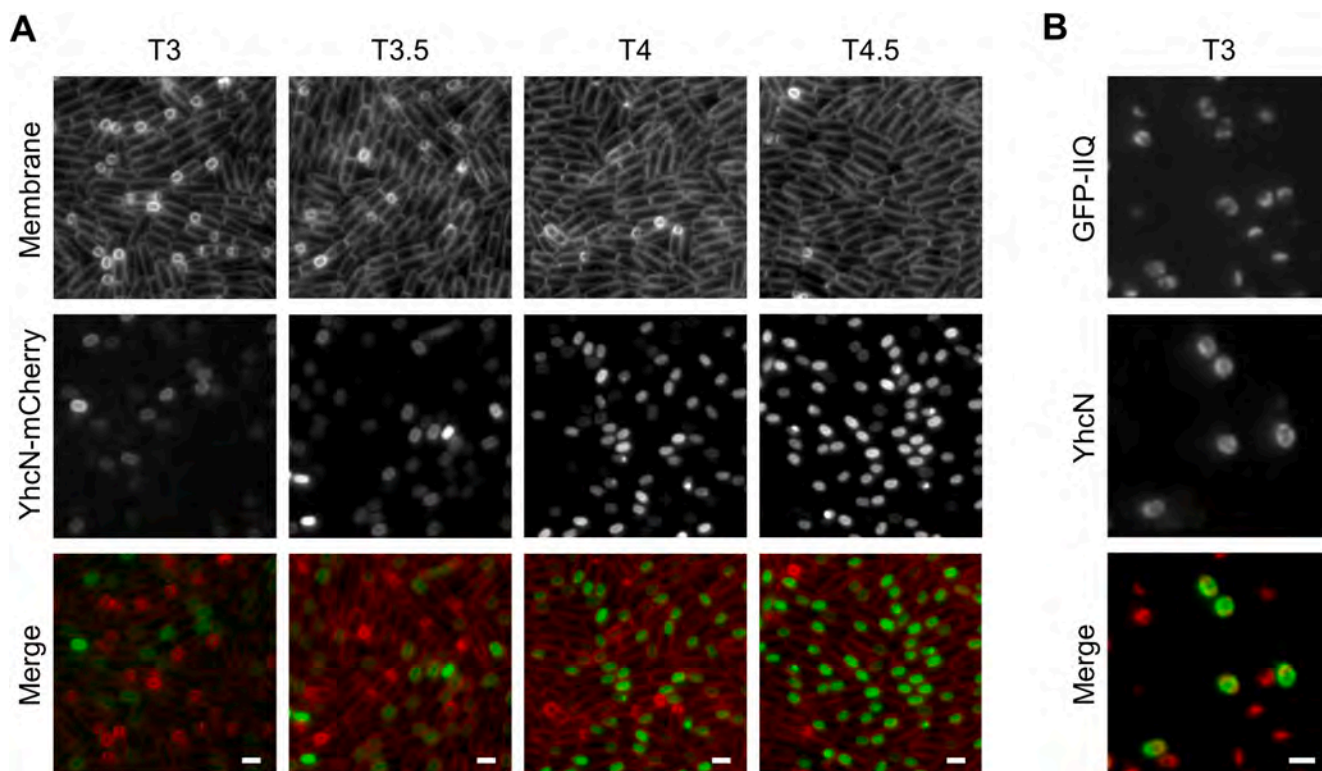
Fig. 1. YhcN localizes uniformly around the forespore. A. Representative images of YhcN-mCherry localization during a sporulation time-course. The mCherry signal is false-coloured green in the merged images. Cell membranes were visualized with the TMA-DPH fluorescent dye and are false-coloured red in the merged images. **B.** Immunofluorescence localization of YhcN observed 3 h after the onset of sporulation. *B. subtilis* cells expressing a GFP-SpoIIQ (GFP-IIQ) fusion protein were labeled using anti-YhcN serum and secondary Cy3-conjugated anti-rabbit IgG. The GFP and Cy3 signals are false-coloured red and green, respectively, in the merged image. Scale bars, 1 μm.

decreased from 59% ($\pm$19%, n = 3) in the $\Delta cotE$ background to 53% ($\pm$12%, n = 3) in the $\Delta cotE$ $\Delta yhcN$ double mutant (Fig. 2B). Altogether, these results indicate that YhcN is not a major player in spore development and likely has a non-essential role in spore germination, outgrowth and colony-forming ability.

2.2. YhcN displays structural similarities with RBM domains

To get structural insights into the soluble domain of YhcN, we produced a recombinant construct encompassing residues Ala24 to Glu189 (Fig. 3A) as a His$_6$-SUMO fusion (HS-YhcN$_{A24-E189}$) and purified it to homogeneity (see the *Methods* section). The purified YhcN$_{A24-E189}$ protein formed needle-shaped crystals (Fig. 3B) that diffracted to a resolution of 1.77 Å (see Table 1 for data collection and refinement statistics). To solve this structure by molecular replacement, templates were selected according to structural homology predictions performed through the HHpred server. As none of the closest predicted homologues (including SctJ RBM2 from *Salmonella typhimurium*, SctJ RBM2 from *Escherichia coli* EPEC, SpoIIIAH from *B. subtilis* and MamB from *Desulfamplus magnetovallimortis*) yielded a structure solution, we performed *ab initio* phasing. *Ab initio* phase determination was achieved by locating three helices of 14 residues using the ARCIMBOLDO_LITE program (http://chango.ibmb.csic.es/) (Sammito et al., 2013). The high quality of the first model obtained with this strategy allowed building a YhcN model from residue Arg79 to Pro186 but no electron density was observed from Ala24 to Asp78. Mass spectrometry analysis of dissolved crystals provided an experimental molecular weight of 18,703 Da (theoretical value of 18,702 Da), indicating that the N-terminal region of YhcN had not suffered from proteolytic degradation. We therefore deduce that the absence of electron density for the region encompassing residues Ala24 to Asp78, which is not predicted to contain any

secondary structure (prediction performed using the Jpred 4 server, https://www.compbio.dundee.ac.uk/jpred/), is due to flexibility in the crystal.

YhcN crystal structure contains a three-stranded β-sheet (β1β2β3) packed against two α-helices (α1α2) on one side and two C-terminal α-helices (α3α4) on the other side (Fig. 3C). Its overall fold resembles RBMs displaying the αββαβ topology. Consistent with this, the DALI server detected structural similarities between YhcN and RBMs found in inner membrane components of various secretion systems (Morlot and Rodrigues, 2018; Spreter et al., 2009). The α1β1β2α2β3 region of YhcN aligns best with the RBM domain of SpoIIIAH from *B. subtilis* (PDB entry 3UZ0, RMSD (root-mean-square deviation) of 1.78 Å, 15% sequence identity, 32% sequence similarity over 64 residues) (Fig. 3D). It superimposes to a lesser extent onto the RBM2 of SctJ from *S. typhimurium* (PDB entry 5TCP, RMSD of 2.41 Å, 10% sequence identity, 30% sequence similarity over 64 residues) (Fig. 3E), the RBM2 of FliF from *S. typhimurium* (PDB entry 6SD2, RMSD of 2.42 Å, 21% sequence identity, 33% sequence similarity over 69 residues) (Fig. S4A), the RBM2 of SctD from *S. typhimurium* (PDB entry 5TCP, RMSD of 2.51 Å, 7% sequence identity, 32% sequence similarity over 63 residues) (Fig. S4B), the RBM core of *B. subtilis* SpoIIIAG (PDB entry 5WC3, RMSD of 2.64 Å, 13% sequence identity, 31% sequence similarity over 64 residues) (Fig. S4C) and SpoIIIAF (PDB entry 6DCS, RMSD of 3.89 Å, 7% sequence identity, 21% sequence similarity over 65 residues) (Fig. S4D). The structural similarities between YhcN and ring-forming domains found in secretion systems suggest that YhcN might be a component of a new transport system, or a ring-forming protein that might have evolved toward a new function (see the *Discussion* section).

More intriguingly, the DALI server also detected structural similarities between YhcN and the C-terminal metal-binding domain of MamM from *Magnetospirillum gryphiswaldense* (PDB entry 6H8A, r.m.s.d. of 3.03
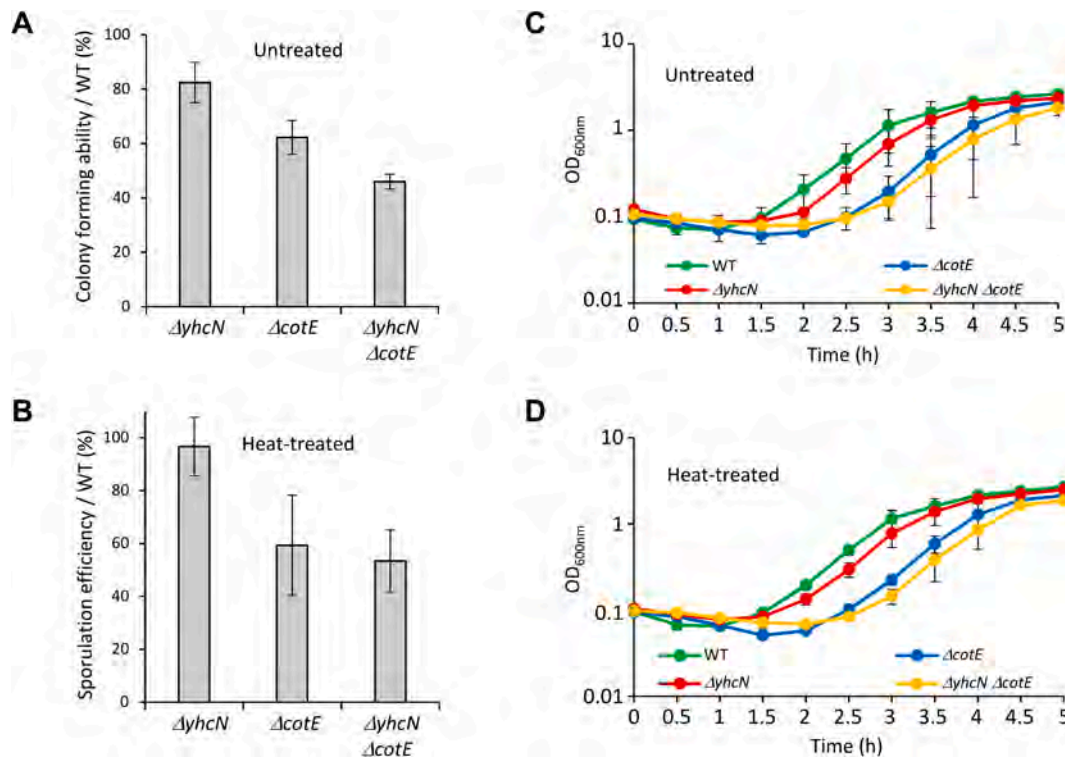
Fig. 2. YhcN is mildly involved in spore outgrowth and colony formation. A-B. Average colony-forming ability of spores (±STDEV, n = 3) (**A**) or sporulation efficiency (±STDEV, n = 3) (**B**) of Δ*yhcN* (bHC120), Δ*cotE* (bHC77) and Δ*yhcN* Δ*cotE* (bHC126) cells relative to wild-type cells (bDR2413). For colony-forming ability assays (**A**), purified spores were plated onto solid medium without heat treatment. For sporulation efficiency assays (**B**), spores were collected 24 h after the onset of sporulation and were treated at 80 °C for 20 min prior to plating onto solid medium. **C–D.** Average outgrowth time-course (±STDEV, n = 2) of untreated (**C**) and heat-treated (**D**) wild-type (WT, bDR2413, green curve), Δ*yhcN* (bHC120, red curve), Δ*cotE* (bHC77, blue curve) and Δ*yhcN* Δ*cotE* (bHC126, yellow curve) spores in nutrient-rich medium (LB), monitored by measuring the optical density at 600 nm (OD$_{600nm}$). Optical density first decreases during spore germination and then increases during outgrowth and vegetative growth.
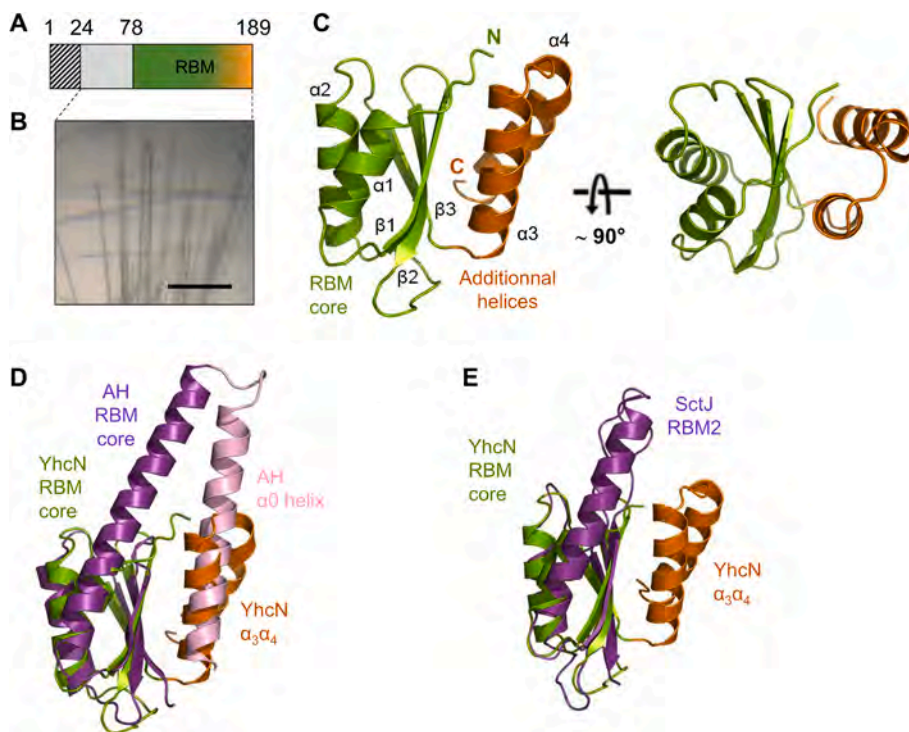

Fig. 3. Ab initio crystal structure of YhcN from *B. subtilis*. A. Domain structure of YhcN from *B. subtilis* showing the lipobox (hatched area), the invisible flexible region in the crystal structure (in grey) and the RBM domain (green to orange shade). **B.** Needle-shaped crystals of YhcN obtained in 100 mM HEPES pH 7.5, 20% (w/v) PEG 8,000. Scale bar, 100 μm. **C.** Ribbon representation of YhcN with the RBM core coloured in green and the two additional C-terminal α-helices coloured in orange. β-strands, α-helices, N- and C-termini are labeled. **D.** Overlay of YhcN with SpoIIIAH from *B. subtilis* (PDB entry 3UZ0). The RBM cores of YhcN and SpoIIIAH are respectively coloured in green and violet, and their additional secondary structures are respectively coloured in orange and pink. **E.** Overlay of YhcN with the second periplasmic RBM (RBM2) domain of *S. typhimurium* SctJ (PDB entry 5TCP, in violet).

Table 1
Data collection and refinement statistics.

Data collection	
Name of dataset	4YhcN_A2_1
X-ray source	ID30A-3 (ESRF)
Wavelength (Å)	0.9677
Scan range (°)	250
Oscillation (°)	0.1
Space group	$P2_12_12_1$
Unit-cell parameters	
a, Å	31.48
b, Å	52.28
c, Å	134.13
α, °	90.00
β, °	90.00
γ, °	90.00
Number of molecules in ASU	2
Resolution (last shell), Å	1.77 (1.77–1.87)
Completeness, %	98.3 (98.4)
I/σ(I)	13.16 (2.75)
Rsym[†], %	6.6 (55.7)
Unique reflections	22,053 (3,302)
Observed reflections [I/σ(I) > 1]	102,053 (15,716)
Wilson B factor, (Å²)	35.01
DIRECT *ab initio* PHASING	
ARCIMBOLDO model (residues)	209
Correlation coefficient (%)	40.76
Refinement and model statistics	
Resolution (last shell), Å	1.77 (1.77–1.82)
R-factor[‡], R-free[§]	0.205, 0.234
rmsd from target[i]	
Bond lengths, Å	0.009
Bond angle, °	1.193
Mean B factor (Å²)	41.57
Ramachandran plot[**]	
Core, %	93.2
Allowed, %	6.8
Disallowed, %	0

Values in parentheses are for the outermost shell of data.

[†] Rsym = (Σ(ABS(I(h,i) − (I(h))))/(Σ(I(h,i))).

[‡] R-factor = ΣjjFoj – jFcjj/ΣjFoj where Fo and Fc are the observed and calculated structure factor amplitudes, respectively.

[§] R-free is the R-factor calculated with 5% of the reflections chosen at random and omitted from refinement.

[**] Performed by Procheck.

[i] rmsd of bond lengths and bond angles from ideal geometry.

Å, 12% sequence identity, 35% sequence similarity over 695 residues) (Fig. S4E), which belongs to the family of cation diffusion facilitators that control metal cation homeostasis (Cotrim et al., 2019). However, YhcN does not possess a transmembrane transport domain as found in MamM, no metal ion was detected in the crystal structure of YhcN and none of the MamM metal-binding residues are conserved in YhcN. It thus appears unlikely that YhcN is a homologue of MamM C-terminal domain.

2.3. YhcN and SpoIIIAH do not form rings in vitro

Although the region encompassing residues Arg79 to Asn150 in YhcN resembles RBM cores found in ring-forming proteins, no YhcN oligomer was detected in the crystal structure or in solution. The asymmetric unit of YhcN$_{A24-E189}$ contains two molecules whose interface buries a surface of 389.8 Å². The contacts between the two YhcN molecules only involve electrostatic interactions, which likely result from crystal packing (Fig. 4A–B). In addition, YhcN$_{A24-E189}$ in solution was detected as a monomer by SEC-MALLS analysis (apparent molecular weight of 21.04 ± 1.24 kDa, Fig. 4C).

Furthermore, when the YhcN crystal structure is superimposed onto one protomer of the SctJ RBM2 or SpoIIIAG homodimers observed in oligomeric rings, the two C-terminal α-helices of YhcN overlay the adjacent SctJ or SpoIIIAG protomer (Fig. 4D–E). A steric hindrance of

the canonical RBM oligomerization interface is also observed in the *B. subtilis* SpoIIIAH protein, which contains a N-terminal helix that packs against the β-sheet of the RBM core (Fig. 4G–H) (Levdikov et al., 2012; Meisner et al., 2012; Morlot and Rodrigues, 2018). Based on the structural similarities between SpoIIIAH and the SctJ family of proteins, SpoIIIAH was proposed to form a homomeric ring oligomer but so far, SpoIIIAH was only detected as a monomer in solution (Levdikov et al., 2012; Meisner et al., 2012). We thus reasoned that shielding of the ring oligomerization interface by additional secondary structures in YhcN and SpoIIIAH might be the reason why these proteins are not able to form rings *in vitro*.

To investigate this, we produced and purified truncated constructs of YhcN deleted from the two C-terminal α-helices (YhcN$_{A24-N150}$, Fig. 4F) and of SpoIIIAH deleted from the N-terminal region and the α0 helix (AH$_{S129-K218}$, Fig. 4I). SEC-MALLS analysis provided consistent apparent molecular weights of 14.47 ± 0.37 kDa for YhcN$_{A24-N150}$ (theoretical value of 14.25 kDa) (Fig. 5A) and 9.67 ± 0.20 kDa for AH$_{S129-K218}$ (theoretical value of 9.81 kDa) (Fig. S5A). However, both constructs showed very little chemical shift dispersion in the methyl proton region (0 to 1 ppm) and in the amide proton region (8 to 10 ppm) when analyzed by 1D liquid-state NMR (Fig. 5C for YhcN$_{A24-N150}$ and Fig. S5B for AH$_{S129-K218}$). In addition, a λ_{NOE} parameters of 0.75 was calculated for both YhcN$_{A24-N150}$ and AH$_{S129-K218}$ (Fig. 5E and Fig. S5C, respectively), indicating a poor proton density (Schanda et al., 2006). These observations are characteristic of unfolded proteins, showing that proper folding of YhcN and SpoIIIAH RBM cores requires the presence of the flanking additional secondary structures. In parallel, we tested whether truncation of the N-terminal Asn-rich disordered region of YhcN, encompassing residues A24 to N76, would trigger *in vitro* oligomerization by purifying a YhcN$_{D78-E189}$ construct. 1D liquid-state NMR analysis showed a very large chemical shift dispersion in the methyl proton region (0–1 ppm) and in the amide proton region (8–10 ppm), indicative of a very well folded protein (Fig. 5D). Nonetheless, YhcN$_{D78-E189}$ (theoretical molecular weight of 12.7 kDa) was only detected as a low-molecular weight species by SEC-MALLS (15.93 ± 1.0 kDa, Fig. 5B), showing that the presence of the N-terminal Asn-rich region is not what prevents the RBM domain to form rings. If YhcN and SpoIIIAH are ring-forming proteins, it thus appears that their RBM domain is not sufficient to promote ring oligomerization *in vitro*.

2.4. The β-triangle region of SpoIIIAG is required and sufficient for ring formation in vitro

The ring-forming protein SpoIIIAG has a non-conventional RBM domain made of a RBM core (α1β1β8α2β9, encompassing residues K90 to A125 and residues P182 to S229) and a β-triangle region (β2-β7, encompassing residues T126 to K181) (Fig. S5D) (Rodrigues et al., 2016; Zeytuni et al., 2017). The former region forms a ring in which the protomers interact through an interface similar to those observed in RBM2 of SctJ, RBM3 of SctD, and in RBM2 and RM3 of FliF (Bergeron et al., 2015; Johnson et al., 2020; Worrall et al., 2016). The β-triangle region forms a unique tubular structure composed of a β-ring and a β-barrel. The disordered region encompassing residues S51 to K88 was not visible in the cryo-electron microscopy structure of SpoIIIAG$_{K55-S229}$ reported previously and was shown to be unnecessary for SpoIIIAG ring formation (Rodrigues et al., 2016; Zeytuni et al., 2017). To determine which region in SpoIIIAG is required for ring formation, we produced and purified truncated soluble constructs deleted from the β-triangle region (AG$_{S51-S229Δ(L128-K180)}$) or containing only the β-triangle region (AG$_{T126-K181}$).

The AG$_{S51-S229Δ(L128-K180)}$ construct eluted as two main species by gel filtration: a high-molecular-weight species (peak 1 in Fig. S5E-F) and a low-molecular-weight species (peak 2 in Fig. S5E-F). 1D liquid-state NMR performed on peak 2 indicated that the protein is poorly folded (Fig. S5G-H). On the other hand, observation of the protein fraction eluting close to the void volume (peak 1) by negative-stain electron
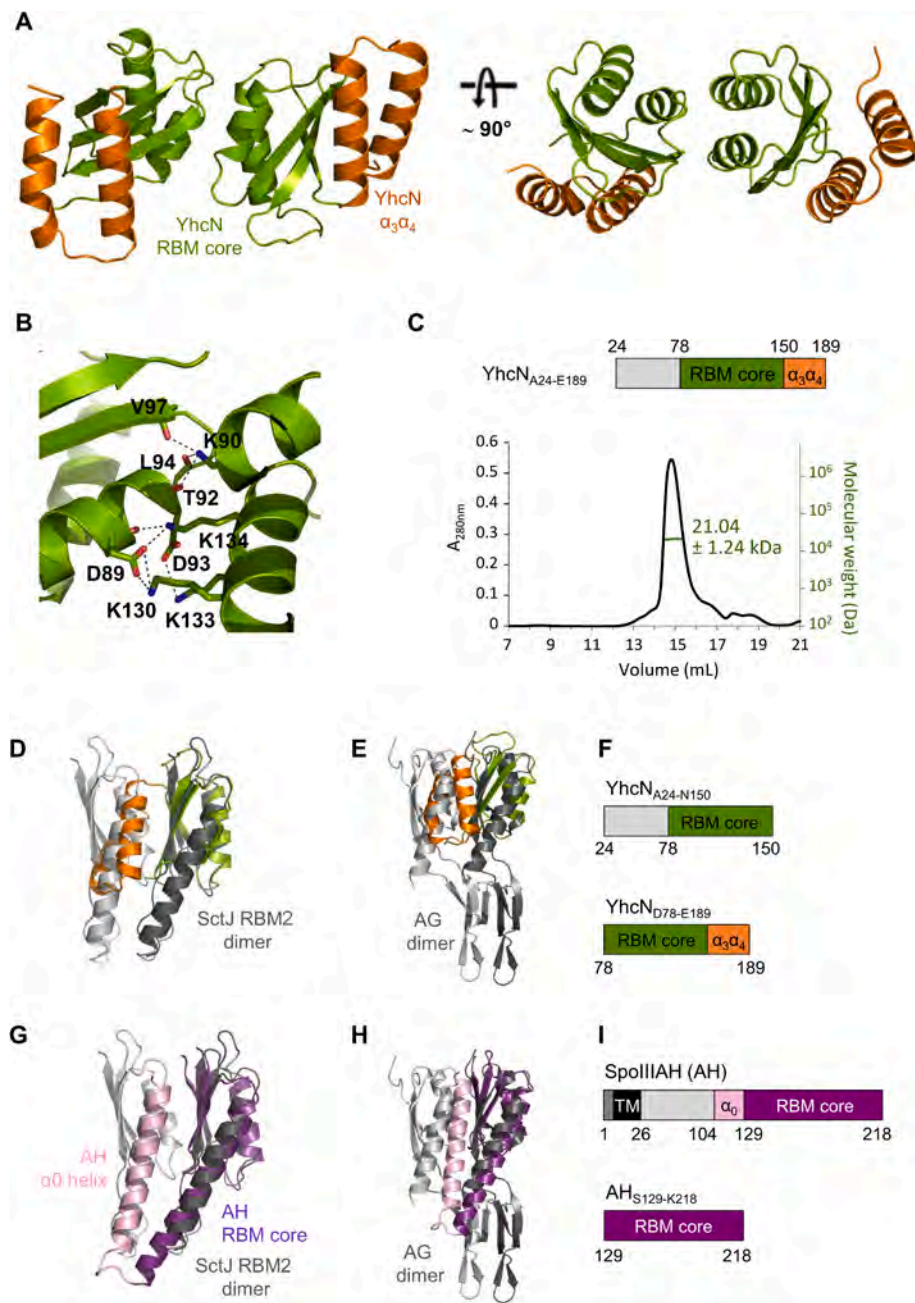
Fig. 4. Analysis of YhcN oligomerization. A. Ribbon representation of the two YhcN molecules present in the asymmetric unit, shown in two different orientations. The YhcN RBM core is coloured in green, the C-terminal α3 and α4 helices are coloured in orange. **B.** Close-up view of the electrostatic interactions established by the two molecules of YhcN in the asymmetric unit. Residues involved in the intermolecular contacts are labeled and shown as atom-coloured sticks. **C.** SEC-MALLS analysis of YhcN$_{A24-E189}$ (SEC650 column). Chromatograms are displayed with the absorbance at 280 nm (A$_{280nm}$) as a black line and arbitrary units displayed on the left axis, and molecular weight estimation as a green line with values (in Da) displayed on the right axis. The estimated average molecular weight is detailed on the graph. **D-E.** Ribbon representations of YhcN (RBM core in green, C-terminal helices in orange) superimposed onto two adjacent protomers from the ring formed by SctJ RBM2 from *S. thyphimurium* (**D**, PDB entry 5TCP, in light and dark grey) or from the ring formed by SpoIIIAG from *B. subtilis* (**E**, PDB entry 5WC3, in light and dark grey). **F.** Schematics of the truncated constructs of YhcN showing the flexible region invisible in the crystal structure (in grey), the RBM core (in green) and the C-terminal α3 and α4 helices (in orange). **G–H.** Ribbon representations of SpoIIIAH (AH) from *B. subtilis* (PDB entry 3UZ0, RBM core in violet, α0 N-terminal helix in pink) superimposed onto two adjacent protomers from the ring formed by SctJ RBM2 from *S. thyphimurium* (**G**, PDB entry 5TCP, in light and dark grey) or from the ring formed by SpoIIIAG from *B. subtilis* (**H**, PDB entry 5WC3, in light and dark grey). Note that the additional secondary structures of the RBM domains of YhcN and SpoIIIAH (in orange and pink, respectively) hinder the canonical oligomerization interface of SctJ RBM2 and of the SpoIIIAG RBM core. **I.** Schematics of the truncated constructs of SpoIIIAH showing the invisible flexible region in the crystal structure (in grey), the RBM core (in violet) and the N-terminal α0 helix (in pink).

microscopy showed that it mainly contains large aggregates (Fig. S5I). The β-triangle region of SpoIIIAG thus appears to be required for proper folding of the protein and thus for ring oligomerization.

By contrast the AG$_{T126-K181}$ construct, which contains only the β-triangle region, formed rings, as observed by negative-stain electron microscopy (Fig. 5G). Due to the heterogeneity and large polydispersity of this sample, no apparent molecular weight could be deduced from SEC-MALLS analysis. However when we measured the dimensions of the SpoIIIAG$_{T126-K181}$ rings, their inner diameter was similar (~8 nm) to the inner diameter of AG$_{S51-S229}$ rings (Rodrigues et al., 2016; Zeytuni et al., 2017), suggesting that the β-triangle region of SpoIIIAG is sufficient to form the 30-mer β-barrel observed previously (Rodrigues et al., 2016; Zeytuni et al., 2017).

Altogether, these observations indicate that the β-triangle region of SpoIIIAG is necessary and sufficient for ring formation while the RBM core region is not sufficient to promote SpoIIIAG oligomerization *in vitro*. In SpoIIIAG, the RBM core might thus rather play a role in stabilizing the

ring than in initiating its oligomerization.

3. Discussion and conclusions

The structural characterization of the YhcN protein reported here reveals a new RBM domain involved in spore germination. YhcN contains a disordered N-terminal region, a RBM core made of a three-stranded β-sheet packed against two α-helices, and two additional C-terminal α-helices. Despite the presence of the RBM core and similar to the RBM-containing sporulation protein SpoIIIAH, YhcN does not oligomerize *in vitro*. Nonetheless, *in vivo*, the assembly of SpoIIIAH rings might be triggered by the membrane environment, including membrane anchoring and/or contacts with A-Q proteins. Regarding YhcN, its cellular context, such as N-terminal lipidation and yet-to-be identified partners, might also be required for ring formation. More specifically, one might speculate that upon interaction with partner(s), the C-terminal α3 and α4 helices could move away from the RBM core, exposing
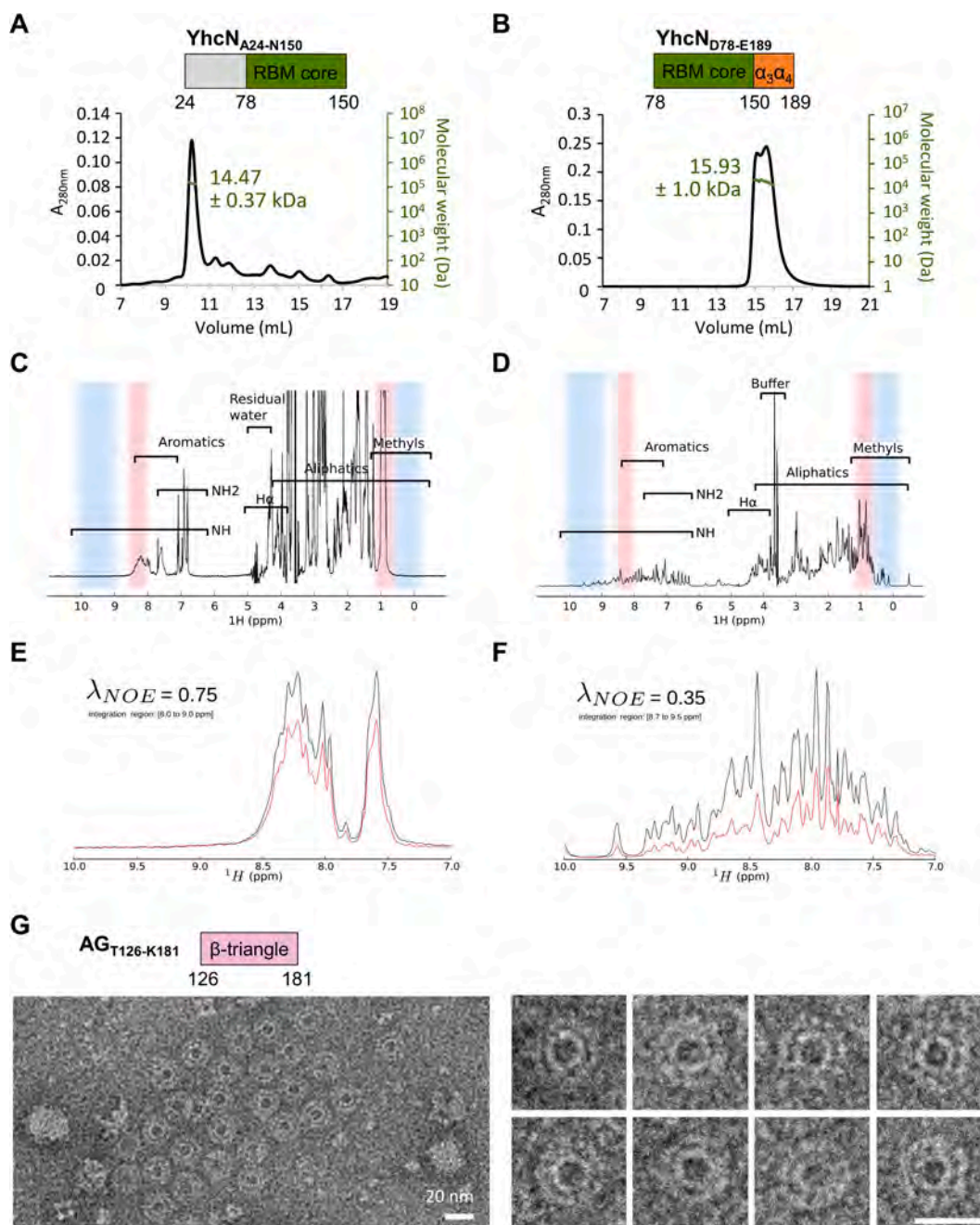
Fig. 5. Analysis of the oligomerization ability of YhcN and AG truncated constructs. A–B. SEC-MALLS analysis of YhcN$_{A24-N150}$ (**A**, Superdex 75 column) and YhcN$_{D78-E189}$ (**B**, SEC650 column). Chromatograms are displayed with the absorbance at 280 nm (A$_{280nm}$) as a black line and arbitrary units displayed on the left axis, and molecular weight estimation as a green line with values (in Da) displayed on the right axis. The estimated average molecular weight is detailed on the graph. **C–D.** 1D ^{1}H NMR spectra of YhcN$_{A24-N150}$ (**C**) and YhcN$_{D78-E189}$ (**D**) showing zones in which the signal arises from folded (blue shadows) or random coil (pink shadows) regions. The graph zones corresponding to protons linked to carbons of the main chain (Hα), protons located in NH, NH$_2$, aromatic, aliphatic and methyl groups, or protons from the buffer and water are also indicated. **E–F.** Overlays of 1D reference (black) and saturated (red) spectra for YhcN$_{A24-N150}$ (**E**) and YhcN$_{D78-E189}$ (**F**). The λ$_{NOE}$ parameter is an independent measurement of the compactness of the protein. A value of 0.75 reveals a low proton density due to an unfolded protein conformation. By contrast, the λ$_{NOE}$ parameter of 0.35 indicates a high proton density that corresponds to a well folded protein. **G.** Negative-stain electron microscopy analysis of the truncated construct of SpoIIIAG containing only the β-triangle region (AG$_{T126-K181}$). Large field (left panel) and close-up (right panel) views show the presence of rings. Scale bars throughout, 20 nm.

an oligomerization interface. Since the YhcN$_{A24-N150}$ construct does not form rings, it is unlikely that this putative oligomerization interface consists in the RBM core alone, but it might involve both the RBM core and the C-terminal α-helices. As DPA release is affected in the absence of YhcN (Johnson and Moir, 2017), putative partners might include SpoVA and SpoVV components of the DPA channel (Ramírez-Guadiana et al., 2017; Setlow, 2014).

Somewhat intriguingly, however, while RBM domains have been proposed to promote ring formation, only a few RBM-containing proteins have been shown to form ring-like structures when produced in a heterologous system and isolated from physiological protein partner(s). Those proteins include the SpoIIIAG component from the SpoIIIA-SpoIIQ sporulation complex in *B. subtilis*, the FliF component of the *S. thyphimurium* flagellum and various secretins from type-II and type III

secretion systems (Chami et al., 2005; Hay et al., 2017; Howard et al., 2019; Johnson et al., 2020; Rodrigues et al., 2016; Tosi et al., 2014; Yan et al., 2017). All these proteins contain a RBM core and an additional region that assembles into a homo-oligomeric β-barrel. In this work, we show that the β-barrel domain is required and sufficient for SpoIIIAG ring formation, suggesting that β-barrel regions are critical determinants for the oligomerization of RBM-containing proteins *in vitro*. On the other hand, proteins that only contain RBM core domains form recombinant oligomeric rings in very rare cases. For example, the highly conserved SctJ and SctD components of the inner membrane platform of T3SS do not oligomerize when produced out of their native environment (Bergeron et al., 2015, 2013; Spreter et al., 2009). To our knowledge, the only recombinant construct forming rings of RBM domains is the one containing the N0, N1 and N2 subdomains of the XcpQ secretin from *Pseudomonas aeruginosa* (Douzi et al., 2017). Less obviously, the SctJ component of *E. coli* T3SS forms a helical assembly *in crystallo* (Yip et al., 2005).

In this context, one might thus question the term "ring-building-motif" that was attributed to this fold. While these motifs might be prone to oligomerize, proper ring formation seems to require an additional region, the cellular environment and/or protein partners in many cases. In the case of RBM-containing proteins that have not yet been shown to form ring oligomers in their cellular context, an alternative hypothesis is that their RBM domain(s) might have evolved to fulfill different roles. The acquisition of additional secondary structures might for example have allowed these proteins to establish interactions with yet-to-be identified heteromeric partner(s). Finally, regarding YhcN, which has so far not been involved in any transport machinery, we cannot exclude that its αββαβ fold results from a convergent structural evolution. In other words, YhcN function might be totally unrelated to the ring-forming function of RBM found in secretion proteins. Instead, the structure of its globular domain might have converged towards a RBM, whose fold appears to be rather simple.

In this regard, the outgrowth phenotype of *yhcN* mutant spores calls to mind the phenotype caused by mutations in the gene coding for the germination protease (GPR), which initiates degradation of SASPs in the forespore (Sanchez-Salas and Setlow, 1993). In support of this idea, YhcN harbors a high content of asparagine residues (16.4% over the whole protein sequence), as observed in SASPs, and displays a KLEVADE sequence, which is reminiscent of the KLEIASE sequence responsible for the recognition and degradation of SASPs by the GPR protease (Bagyan et al., 1998; Setlow, 1988). In that respect, it is interesting to note that *yhcN* is in an operon with the *yhcO* gene (Fig. S1) (Eichenberger et al., 2004; Steil et al., 2005), whose mRNA is also detected in spores (Korza et al., 2019), and that codes for a protein with strong structural similarity to the peptidase domain of collagenases from *Clostridium tetani* and *Clostridium histolyticum* (Eckhard et al., 2013). It is thought that the amino acids released from SASP degradation are important for the reactivation of protein synthesis during outgrowth (Sanchez-Salas and Setlow, 1993; Traag et al., 2013). While it is unlikely that YhcN *per se* forms a transporter, it is tempting to speculate that the protein is part of a transport system that allows amino acids released from extracellular proteins to be used for protein synthesis during outgrowth. In other words, amino acids released from both internal (via SASP proteases) and external sources (via YhcN/YhcO) would be used for germination and outgrowth.

4. Methods

4.1. Bacterial strains and plasmids

Strains, plasmids and oligonucleotides used in this study are listed in Table S1. All *B. subtilis* strains were derived from the prototrophic strain PY79 (Youngman et al., 1983).

4.2. Fluorescence microscopy

Live-cell epifluorescence microscopy was performed using a Zeiss Axioplan 2 microscope equipped with 100x objective N/A 1.4. A 250 μL aliquot of sporulating cells at the desired time-point was pelleted by centrifugation and then resuspended in 10 μL of resuspension medium containing the membrane dye TMA-DPH (1-(4-trimethylammonium-phenyl)-6-phenyl-1,3,5-hexatriene *p*-toluenesulfonate) (0.05 mM). A 2 μL aliquot of the cell suspension was spread on a 2% (w/v) agarose pad prepared in resuspension medium set using a gene frame (Bio-Rad), and then covered with a glass coverslip (#1.5) for imaging. CFP and GFP fluorescence was acquired using an exposure time of 800 ms, and YFP, mCherry and TMA-DPH fluorescence was acquired using an exposure time of 400 ms.

Immunostaining was adapted from Harry et al. (Harry et al., 1995). Bacteria were fixed for 15 min at room temperature (RT) and 35 min on ice with 2% (v/v) paraformaldehyde, 0.02% glutaraldehyde (Electron Microscopy Sciences) in 10 mM PBS pH 7.5, washed three times in PBS and resuspended in 50 mM glucose, 20 mM Tris-HCl pH 7.5, 10 mM EDTA. Lysozyme was added to a final concentration of 2 mg·ml^{-1} and cells were transferred onto multiwell slides coated with poly L-lysine (Sigma). The slides were air-dried and treated for 5 min with methanol (-20 °C) and 30 sec with acetone (-20 °C). After air drying, the wells were pre-treated with 2% (w/v) bovine serum albumin in PBS (BSA-PBS) for 30 min at RT prior to incubation for 1 h with a 1:200 dilution of anti-YhcN rabbit antibodies (Covalab) in BSA-PBS. The slides were then washed 10 times with PBS and incubated for 1 h with a 1:200 dilution of Cy3-conjugated goat anti-rabbit immunoglubulin G (Jackson Immunoresearch) in BSA-PBS. After extensive wash with PBS, the slides were mounted using Vectashield antifade mounting medium (Vectorlabs). Samples were observed with a two-deck Olympus IX83 optical microscope equipped with a UPFLN 100X O-2PH/1.3 objective and an ORCA-Flash4.0 Digital sCMOS camera from Hamamatsu. Images were acquired using the Volocity software package.

4.3. Spore outgrowth, colony-forming ability and sporulation efficiency assays

For spore outgrowth and colony-forming ability assays, spores from 25 mL of sporulating wild-type (bAT87), Δ*yhcN* (bHC120), Δ*cotE* (bHC77) or Δ*yhcN* Δ*cotE* (bHC126) cells (induced by resuspension) were harvested by centrifugation 27 h after the onset of sporulation. Spores were washed with 20 mL of MilliQ H$_2$O and treated with lysozyme (1.2 mg·mL^{-1}) at 37 °C for 1 h. SDS was added to a final concentration of 2% and spores were incubated for a further 20 min at 37 °C. Spores were harvested by centrifugation and then washed seven times with 20 mL of MilliQ H$_2$O.

Spore outgrowth time courses were performed by inoculating 25 mL of LB medium with purified spores to an initial optical density at 600 nm (OD$_{600nm}$) of approximately 0.1. Spore suspensions were either heat-treated (80 °C for 20 min) or untreated prior to incubation at 37 °C with aeration. Spore germination and outgrowth were monitored for two biological replicates per strain by measuring OD$_{600nm}$ over time. Colony-forming ability of spores was determined as the total number of CFUs (colony-forming units) compared with wild-type CFUs from purified spores plated on LB agar without heat treatment. Sporulation efficiency was determined in 24–30-h cultures as the total number of heat-resistant (80 °C for 20 min) CFUs compared with wild-type heat-resistant CFUs.

4.4. Protein production and purification

The N-terminus of all recombinant constructs were fused to a hexahistidine tag followed by the SUMO cleavage site of the Ulp1 protease (His-SUMO tag) (Marblestone et al., 2006) and produced in *E. coli* BL21 (*DE3*) STAR cells. Cells were grown at 37 °C under agitation (180 RPM)

in 2-L baffled flasks containing 500 mL of Terrific Broth medium (BD Biosciences) supplemented with ampicillin (100 μg·mL^{-1}) until the OD$_{600nm}$ reached 0.8. After the cultures were cooled to 25 °C, production of recombinant proteins was induced with 0.5 mM IPTG (isopropyl β-D-1-thiogalactopyranoside) and cultures were further grown for 18 h at 25 °C. Following centrifugation, cell pellets were resuspended in 1/40th volume of a lysis buffer containing the Complete™ cocktail of protease inhibitors (Roche), 50 mM Tris-HCl pH 8.0, 500 mM NaCl, 25 mM imidazole and 10% (v/v) glycerol. Cells lysis was performed using a cell disruptor (Microfluidics) at 15 kPsi, and cell debris were pelleted by centrifugation at 40,000 × g for 30 min at 4 °C. The centrifugation supernatant was loaded on a 8-mL Ni-NTA agarose resin (Qiagen) equilibrated with the lysis buffer. After extensive washing, the fusion protein was eluted with a linear 0–100% gradient of elution buffer (50 mM Tris-HCl pH 8.0, 300 mM NaCl, 500 mM imidazole, 10% (v/v) glycerol) over 10 column volumes. Elution fractions were pooled, mixed with a 1:200 M ratio of a His-tagged Ulp1 protease sample (Uehara et al., 2010), and dialyzed overnight at 4 °C against 100 volumes of dialysis buffer (50 mM Tris-HCl pH 8.0, 300 mM NaCl, 10% (v/v) glycerol). Cleavage reactions were loaded onto a 8-mL Ni-NTA resin to remove the His-SUMO tag and His-Ulp1, and the untagged protein was collected in the flow through fractions. Pooled flow-through fractions were concentrated with Amicon Ultra Centrifugal Units with a molecular weight cutoff of 3 or 10 kDa (Millipore) and were injected onto an Enrich™ SEC650 10 × 300 gel-filtration column (Biorad). Proteins were eluted in 25 mM Tris-HCl pH 8.0, 150 mM NaCl, and concentrated before protein concentration was measured using absorbance at 280 nm.

4.5. Mass spectrometry analyses

Protein samples were denatured and diluted to 5 μM in 0.03% TFA. Four μL of cooled samples (10 °C) were first desalted using a reverse phase-C8 cartridge (Zorbax 300SB-C8, 5um, 300 μm ID × 5 mm, Agilent Technologies) and eluted in 67% acetonitrile, 0.03% TFA, for mass spectrometry detection. Liquid Chromatography Electrospray Ionization Mass Spectrometry (LC/ESI-MS) analysis was performed using a 6210 LC/ESI-TOF mass spectrometer interfaced with an HPLC binary pump system (Agilent Technologies). Mass spectra were recorded in the 300–3200 m/z range, in the positive ion mode with spectra in the profile mode. The MS spectra were acquired and the data processed with the MassHunter workstation software (v. B.02.00, Agilent Technologies) and with the GPMAW software (v. 7.00b2, Lighthouse Data, Denmark).

4.6. NMR analyses

Conventional ^{1}H 1D NMR and 1D HET-SOFAST experiments were performed on a 700 MHz spectrometer (Bruker Avance III HD Liquid) equipped with a triple resonance cryo-probe. Quantitative compactness measurements (Schanda et al., 2006) were obtained recording two 1D HET-SOFAST data sets with and without a band-selective inversion pulse covering the aliphatic region. Data were acquired at 25 °C and processed using the Topspin3.5 software (Bruker, Inc.) and the NMRlib library (Favier and Brutscher, 2019). The time domain data were multiplied with a 90° phase-shifted sine-bell apodization function and zero-filled to 8192 complex data points prior to Fourier transformation. The reference and saturated intensities were obtained by integrating the spectra from 8.5 to 9.5 ppm.

4.7. SEC-MALLS analyses

SEC-MALLS analyses were performed using ENrich^{TM} SEC650 (Biorad) or Superdex 75 (Pharmacia) 10x300 gel-filtration columns connected to an analytic system including a L2130 pump (Hitachi), an Elite LaChrom L-2400 UV detector (Hitachi), an Optilab T-rEX refractometer (Wyatt technologies) and a DAWN HELEOS-II multi angle laser light scattering detector (Wyatt technologies). The column and the systems

were equilibrated in 10 column volumes of 25 mM Tris-HCl pH 8.0, 150 mM NaCl. Fifty μl of protein samples concentrated at a minimum of 2 mg·mL^{-1} were injected with a flow rate of 0.5 mL·min^{-1}. Protein concentration was quantified online by measuring the differential refractive index and using an averaged refractive index increment dn/dc of 0.185 mL·g^{-1}. Accurate weight-averaged molar mass determination was performed with the Astra 6 software (Wyatt Technologies) and curves were represented with Excel (Microsoft office 2013).

4.8. Negative-stain electron microscopy

The protein concentration was adjusted to 0.05 mg·mL^{-1} in 25 mM Tris-HCl pH 8.0, 150 mM NaCl, before preparation of samples using the negative-stain Mica-carbon Flotation Technique (MFT). Samples were absorbed on the clean side of a carbon film on mica, stained with 2% (w/v) sodium silico tungstate. Samples were then transferred to a 400-mesh copper grid, which was subsequently air-dried. Images were taken with defocus values between 1.2 and 2.5 μm on a Technai 12 FEI LaB6 electron microscope operating at 120 kV accelerating voltage. Images were acquired with a calibrated nominal magnification of 30,000, using a CCD Gatan ORIUS SC1000 camera (Gatan, Inc.).

4.9. Protein crystallization and X-ray data collection

High-throughput crystallization trials were performed with a Cartesian PixSys 4200 crystallization robot (Genomic Solutions, U.K.). Hanging drops containing 100 nl of protein (48, 24 or 12 mg·mL^{-1}) and 100 nl of reservoir solution were set up in 96-well Crystal Quick plates (Greiner) and incubated at 20 °C. Initial crystal hits were refined manually by setting up hanging drops containing 1 μL of purified YhcN$_{A24-E189}$ sample (48 or 24 mg/ml) and 1 μL of reservoir solution in 24-well plates (Molecular Dimensions) incubated at 20 °C. Needle-shaped crystals (dimensions of about 20 × 20 × 100 μm) were finally obtained within 2 days in 100 mM HEPES pH 7.5, 20% (w/v) PEG 8,000. Before flash freezing into liquid nitrogen, crystals were soaked for 5 to 30 sec in a cryo-protecting solution containing 100 mM HEPES pH 7.5, 21% (w/v) PEG 8,000 and 15% (v/v) glycerol. X-ray diffraction data were collected at the European Synchrotron Radiation Facility (ESRF, Grenoble, France), on the ID30A-3 (MASSIF-3) beamline. The experimental beamline parameters and data quality of the collected images were monitored with MxCuBE (Gabadinho et al., 2010). Statistics on data collection and refinement are summarized in Table 1.

4.10. Structure determination and refinement

Following indexation and integration of the diffraction data using the XDS program suite (Kabsch, 2010) (see Table 1), *ab initio* phase determination was achieved using the ARCIMBOLDO_LITE program (Sammito et al., 2013) to combine the location of α-helices with PHASER (McCoy et al., 2007) and density modification with SHELXE (Thorn and Sheldrick, 2013). Based on secondary structure predictions performed by the JPRED4 server (http://www.compbio.dundee.ac.uk/jpred/), we searched for three α-helices containing 14 residues in coiled mode, using 27 cores of the Cobalt cluster at the CCRT (http://www-hpc.cea.fr/en/complexe/ccrt.htm.). This strategy yielded a model of high quality, allowing automated building of the YhcN model (from R79 until P186) using Phenix (Terwilliger et al., 2008). The structure of YhcN was completed by cycles of manual building with COOT (Emsley and Cowtan, 2004), addition of water molecules with ARP/wARP (Langer et al., 2008) and refinement with REFMAC (Murshudov et al., 2011), as implemented in the CCP4 program suite. Stereochemical verification was performed with PROCHECK (Laskowski et al., 1993), secondary structures were assigned with DSSP (Kabsch and Sander, 1983) and figures were generated with PyMol (http://www.pymol.org). Coordinates of the final refined model were deposited at the Protein Data Bank (PDB, http://www.rcsb.org) and were assigned PDB entry code

7PEG.

CRediT authorship contribution statement

Bowen Liu: Validation, Formal analysis, Investigation, Visualization. **Helena Chan:** Validation, Formal analysis, Investigation, Visualization, Writing – review & editing. **Elda Bauda:** Validation, Formal analysis, Investigation, Visualization. **Carlos Contreras-Martel:** Validation, Formal analysis, Investigation. **Laure Bellard:** Validation, Investigation. **Anne-Marie Villard:** Validation, Investigation. **Caroline Mas:** Validation, Formal analysis, Investigation, Visualization. **Emmanuelle Neumann:** Validation, Investigation. **Daphna Fenel:** Validation, Investigation. **Adrien Favier:** Validation, Formal analysis, Investigation, Visualization. **Monica Serrano:** Investigation. **Adriano O. Henriques:** Conceptualization, Writing – review & editing, Visualization, Supervision, Project administration. **Christopher D.A. Rodrigues:** Conceptualization, Methodology, Validation, Writing – original draft, Writing – review & editing, Visualization, Supervision, Project administration, Funding acquisition. **Cecile Morlot:** Conceptualization, Methodology, Validation, Writing – original draft, Writing – review & editing, Visualization, Supervision, Project administration, Funding acquisition.

Declaration of Competing Interest

The authors declare that they have no known competing financial interests or personal relationships that could have appeared to influence the work reported in this paper.

Author contributions

AOH, CDAR and CMo designed research; BL, HC, EB, CCM, LB, AMV, CMa, EN, DF, AF and MS performed experiments; BL, HC, EB, CCM, CMa and AF analyzed data; CMo and CDAR wrote the manuscript; HC, AOH, CDAR and CMo revised the manuscript.

Appendix A. Supplementary material

Supplementary data to this article can be found online at https://doi.org/10.1016/j.jsb.2021.107813.

References

Amon, J.D., Yadav, A.K., Ramirez-Guadiana, F.H., Meeske, A.J., Cava, F., Rudner, D.Z., Henkin, T.M., 2020. SwsB and SafA Are Required for CwlJ-Dependent Spore Germination in Bacillus subtilis. J. Bacteriol. 202 (6) https://doi.org/10.1128/JB.00668-19.

Bagyan, I., Noback, M., Bron, S., Paidhungat, M., Setlow, P., 1998. Characterization of yhcN, a new forespore-specific gene of Bacillus subtilis. Gene 212, 179–188. https://doi.org/10.1016/s0378-1119(98)00172-3.

Bagyan, I., Setlow, P., 2002. Localization of the cortex lytic enzyme CwlJ in spores of Bacillus subtilis. J. Bacteriol. 184 (4), 1219–1224. https://doi.org/10.1128/jb.184.4.1219-1224.2002.

Bergeron, J.C., Worrall, L., De, S., Sgourakis, N., Cheung, A., Lameignere, E., Okon, M., Wasney, G., Baker, D., McIntosh, L., Strynadka, N.J., 2015. The Modular Structure of the Inner-Membrane Ring Component PrgK Facilitates Assembly of the Type III Secretion System Basal Body. Structure 23 (1), 161–172. https://doi.org/10.1016/j.str.2014.10.021.

Bergeron, J.R.C., Worrall, L.J., Sgourakis, N.G., DiMaio, F., Pfuetzner, R.A., Felise, H.B., Vuckovic, M., Yu, A.C., Miller, S.I., Baker, D., Strynadka, N.C.J., Kubori, T., 2013. A refined model of the prototypical Salmonella SPI-1 T3SS basal body reveals the molecular basis for its assembly. PLoS Pathog. 9 (4), e1003307. https://doi.org/10.1371/journal.ppat.1003307.

Camp, A.H., Losick, R., 2008. A novel pathway of intercellular signalling in Bacillus subtilis involves a protein with similarity to a component of type III secretion channels. Mol. Microbiol. 69, 402–417. https://doi.org/10.1111/j.1365-2958.2008.06289.x.

Chami, M., Guilvout, I., Gregorini, M., Rémigy, H.W., Müller, S.A., Valerio, M., Engel, A., Pugsley, A.P., Bayan, N., 2005. Structural insights into the secretin PulD and its trypsin-resistant core. J. Biol. Chem. 280 (45), 37732–37741. https://doi.org/10.1074/jbc.M504463200.

Chirakkal, H., O'Rourke, M., Atrih, A., Foster, S.J., Moir, A., 2002. Analysis of spore cortex lytic enzymes and related proteins in Bacillus subtilis endospore germination. Microbiol. Read. Engl. 148, 2383–2392. https://doi.org/10.1099/00221287-148-8-2383.

Costa, T., Steil, L., Martins, L.O., Völker, U., Henriques, A.O., 2004. Assembly of an oxalate decarboxylase produced under sigmaK control into the Bacillus subtilis spore coat. J. Bacteriol. 186, 1462–1474. https://doi.org/10.1128/JB.186.5.1462-1474.2004.

Costa, T.R.D., Felisberto-Rodrigues, C., Meir, A., Prevost, M.S., Redzej, A., Trokter, M., Waksman, G., 2015. Secretion systems in Gram-negative bacteria: structural and mechanistic insights. Nat. Rev. Microbiol. 13 (6), 343–359. https://doi.org/10.1038/nrmicro3456.

Cotrim, C.A., Jarrott, R.J., Martin, J.L., Drew, D., 2019. A structural overview of the zinc transporters in the cation diffusion facilitator family. Acta Crystallogr. Sect. Struct. Biol. 75 (4), 357–367. https://doi.org/10.1107/S2059798319003814.

Douzi, B., Trinh, N.T.T., Michel-Souzy, S., Desmyter, A., Ball, G., Barbier, P., Kosta, A., Durand, E., Forest, K.T., Cambillau, C., Roussel, A., Voulhoux, R., 2017. Unraveling the Self-Assembly of the Pseudomonas aeruginosa XcpQ Secretin Periplasmic Domain Provides New Molecular Insights into Type II Secretion System Secretin Architecture and Dynamics. mBio 8. https://doi.org/10.1128/mBio.01185-17.

Eckhard, U., Schönauer, E., Brandstetter, H., 2013. Structural basis for activity regulation and substrate preference of clostridial collagenases G, H, and T. J. Biol. Chem. 288 (28), 20184–20194. https://doi.org/10.1074/jbc.M112.448548.

Eichenberger, P., Fujita, M., Jensen, S.T., Conlon, E.M., Rudner, D.Z., Wang, S.T., Ferguson, C., Haga, K., Sato, T., Liu, J.S., Losick, R., Jonathan A. Eisen, 2004. The program of gene transcription for a single differentiating cell type during sporulation in Bacillus subtilis. PLoS Biol. 2 (10), e328. https://doi.org/10.1371/journal.pbio.0020328.

Emsley, P., Cowtan, K., 2004. Coot: model-building tools for molecular graphics. Acta Crystallogr. D Biol. Crystallogr. 60 (12), 2126–2132. https://doi.org/10.1107/S0907444904019158.

Favier, A., Brutscher, B., 2019. NMRlib: user-friendly pulse sequence tools for Bruker NMR spectrometers. J. Biomol. NMR 73 (5), 199–211. https://doi.org/10.1007/s10858-019-00249-1.

Filloux, A., Voulhoux, R., 2018. Multiple Structures Disclose the Secretins' Secrets. J. Bacteriol. 200 (5) https://doi.org/10.1128/JB.00702-17.

Gabadinho, J., Beteva, A., Guijarro, M., Rey-Bakaikoa, V., Spruce, D., Bowler, M.W., Brockhauser, S., Flot, D., Gordon, E.J., Hall, D.R., Lavault, B., McCarthy, A.A., McCarthy, J., Mitchell, E., Monaco, S., Mueller-Dieckmann, C., Nurizzo, D., Ravelli, R.B.G., Thibault, X., Walsh, M.A., Leonard, G.A., McSweeney, S.M., 2010. MxCuBE: a synchrotron beamline control environment customized for macromolecular crystallography experiments. J. Synchrotron Radiat. 17 (5), 700–707. https://doi.org/10.1107/S0909049510020005.

Green, E.R., Mecsas, J., 2016. Bacterial Secretion Systems: An Overview. Microbiol. Spectr. 4 (1) https://doi.org/10.1128/microbiolspec.VMBF-0012-2015.

Harry, E.J., Pogliano, K., Losick, R., 1995. Use of immunofluorescence to visualize cell-specific gene expression during sporulation in Bacillus subtilis. J. Bacteriol. 177 (12), 3386–3393. https://doi.org/10.1128/jb.177.12.3386-3393.1995.

Hay, I.D., Belousoff, M.J., Lithgow, T., 2017. Structural Basis of Type 2 Secretion System Engagement between the Inner and Outer Bacterial Membranes. mBio 8. https://doi.org/10.1128/mBio.01344-17.

Higgins, D., Dworkin, J., 2012. Recent progress in Bacillus subtilis sporulation. FEMS Microbiol. Rev. 36 (1), 131–148. https://doi.org/10.1111/j.1574-6976.2011.00310.x.

Howard, S.P., Estrozi, L.F., Bertrand, Q., Contreras-Martel, C., Strozen, T., Job, V., Martins, A., Fenel, D., Schoehn, G., Dessen, A., Kubori, T., 2019. Structure and

assembly of pilotin-dependent and -independent secretins of the type II secretion system. PLoS Pathog. 15 (5), e1007731. https://doi.org/10.1371/journal.ppat.1007731.

Hu, J., Worrall, L.J., Hong, C., Vuckovic, M., Atkinson, C.E., Caveney, N., Yu, Z., Strynadka, N.C.J., 2018. Cryo-EM analysis of the T3S injectisome reveals the structure of the needle and open secretin. Nat. Commun. 9, 3840. https://doi.org/10.1038/s41467-018-06298-8.

Ishikawa, S., Yamane, K., Sekiguchi, J., 1998. Regulation and characterization of a newly deduced cell wall hydrolase gene (cwlJ) which affects germination of Bacillus subtilis spores. J. Bacteriol. 180 (6), 1375–1380. https://doi.org/10.1128/JB.180.6.1375-1380.1998.

Johnson, C.L., Moir, A., 2017. Proteins YlaJ and YhcN contribute to the efficiency of spore germination in Bacillus subtilis. FEMS Microbiol. Lett. 364 https://doi.org/10.1093/femsle/fnx047.

Johnson, S., Fong, Y.H., Deme, J.C., Furlong, E.J., Kuhlen, L., Lea, S.M., 2020. Symmetry mismatch in the MS-ring of the bacterial flagellar rotor explains the structural coordination of secretion and rotation. Nat. Microbiol. 5 (7), 966–975. https://doi.org/10.1038/s41564-020-0703-3.

Kabsch, W., 2010. XDS. Acta Crystallogr. D Biol. Crystallogr. 66 (2), 125–132. https://doi.org/10.1107/S0907444909047337.

Kabsch, W., Sander, C., 1983. Dictionary of protein secondary structure: pattern recognition of hydrogen-bonded and geometrical features. Biopolymers 22 (12), 2577–2637. https://doi.org/10.1002/bip.360221211.

Korotkov, K.V., Gonen, T., Hol, W.G.J., 2011. Secretins: dynamic channels for protein transport across membranes. Trends Biochem. Sci. 36 (8), 433–443. https://doi.org/10.1016/j.tibs.2011.04.002.

Korza, G., Camilleri, E., Green, J., Robinson, J., Nagler, K., Moeller, R., Caimano, M.J., Setlow, P., Henkin, T.M., 2019. Analysis of the mRNAs in Spores of Bacillus subtilis. J. Bacteriol. 201 (9) https://doi.org/10.1128/JB.00007-19.

Kuwana, R., Kasahara, Y., Fujibayashi, M., Takamatsu, H., Ogasawara, N., Watabe, K., 2002. Proteomics characterization of novel spore proteins of Bacillus subtilis. Microbiol. Read. Engl. 148, 3971–3982. https://doi.org/10.1099/00221287-148-12-3971.

Langer, G., Cohen, S.X., Lamzin, V.S., Perrakis, A., 2008. Automated macromolecular model building for X-ray crystallography using ARP/wARP version 7. Nat. Protoc. 3 (7), 1171–1179. https://doi.org/10.1038/nprot.2008.91.

Laskowski, R.A., MacArthur, M.W., Moss, D.S., Thornton, J.M., 1993. PROCHECK: a program to check the stereochemical quality of protein structures. J. Appl. Crystallogr. 26 (2), 283–291.

Levdikov, V.M., Blagova, E.V., McFeat, A., Fogg, M.J., Wilson, K.S., Wilkinson, A.J., 2012. Structure of components of an intercellular channel complex in sporulating Bacillus subtilis. Proc. Natl. Acad. Sci. 109 (14), 5441–5445. https://doi.org/10.1073/pnas.1120087109.

Marblestone, J.G., Edavettal, S.C., Lim, Y., Lim, P., Zuo, X., Butt, T.R., 2006. Comparison of SUMO fusion technology with traditional gene fusion systems: enhanced expression and solubility with SUMO. Protein Sci. Publ. Protein Soc. 15, 182–189. https://doi.org/10.1110/ps.051812706.

McCoy, A.J., Grosse-Kunstleve, R.W., Adams, P.D., Winn, M.D., Storoni, L.C., Read, R.J., 2007. Phaser crystallographic software. J. Appl. Crystallogr. 40 (4), 658–674. https://doi.org/10.1107/S0021889807021206.

McKenney, P.T., Eichenberger, P., 2012. Dynamics of spore coat morphogenesis in Bacillus subtilis. Mol. Microbiol. 83, 245–260. https://doi.org/10.1111/j.1365-2958.2011.07936.x.

Meisner, J., Maehigashi, T., Andre, I., Dunham, C.M., Moran, C.P., 2012. Structure of the basal components of a bacterial transporter. Proc. Natl. Acad. Sci. 109 (14), 5446–5451. https://doi.org/10.1073/pnas.1120113109.

Meisner, J., Wang, X., Serrano, M., Henriques, A.O., Moran, C.P., 2008. A channel connecting the mother cell and forespore during bacterial endospore formation. Proc. Natl. Acad. Sci. 105 (39), 15100–15105. https://doi.org/10.1073/pnas.0806301105.

Morlot, C., Rodrigues, C.D.A., 2018. The New Kid on the Block: A Specialized Secretion System during Bacterial Sporulation. Trends Microbiol. 26 (8), 663–676. https://doi.org/10.1016/j.tim.2018.01.001.

Murshudov, G.N., Skubák, P., Lebedev, A.A., Pannu, N.S., Steiner, R.A., Nicholls, R.A., Winn, M.D., Long, F., Vagin, A.A., 2011. REFMAC5 for the refinement of macromolecular crystal structures. Acta Crystallogr. D Biol. Crystallogr. 67 (4), 355–367. https://doi.org/10.1107/S0907444911001314.

Ramírez-Guadiana, F.H., Meeske, A.J., Rodrigues, C.D.A., Barajas-Ornelas, R.D.C., Kruse, A.C., Rudner, D.Z., Kearns, D.B., 2017. A two-step transport pathway allows the mother cell to nurture the developing spore in Bacillus subtilis. PLoS Genet. 13 (9), e1007015. https://doi.org/10.1371/journal.pgen.1007015.

Riley, E.P., Lopez-Garrido, J., Sugie, J., Liu, R.B., Pogliano, K., 2021. Metabolic differentiation and intercellular nurturing underpin bacterial endospore formation. Sci. Adv. 7 (4) https://doi.org/10.1126/sciadv.abd6385.

Rodrigues, C.D.A., Henry, X., Neumann, E., Kurauskas, V., Bellard, L., Fichou, Y., Schanda, P., Schoehn, G., Rudner, D.Z., Morlot, C., 2016. A ring-shaped conduit connects the mother cell and forespore during sporulation in Bacillus subtilis. Proc. Natl. Acad. Sci. 113 (41), 11585–11590. https://doi.org/10.1073/pnas.1609604113.

Sammito, M., Millán, C., Rodríguez, D.D., de Ilarduya, I.M., Meindl, K., De Marino, I., Petrillo, G., Buey, R.M., de Pereda, J.M., Zeth, K., Sheldrick, G.M., Usón, I., 2013. Exploiting tertiary structure through local folds for crystallographic phasing. Nat. Methods 10 (11), 1099–1101. https://doi.org/10.1038/nmeth.2644.

Sanchez-Salas, J.L., Setlow, P., 1993. Proteolytic processing of the protease which initiates degradation of small, acid-soluble proteins during germination of Bacillus subtilis spores. J. Bacteriol. 175 (9), 2568–2577. https://doi.org/10.1128/jb.175.9.2568-2577.1993.

Schanda, P., Forge, V., Brutscher, B., 2006. HET-SOFAST NMR for fast detection of structural compactness and heterogeneity along polypeptide chains. Magn. Reson. Chem. MRC 44 Spec No, S177-S184. DOI: 10.1002/mrc.1825.

Setlow, P., 2014. Germination of spores of Bacillus species: what we know and do not know. J. Bacteriol. 196 (7), 1297–1305. https://doi.org/10.1128/JB.01455-13.

Setlow, P., 2006. Spores of Bacillus subtilis: their resistance to and killing by radiation, heat and chemicals. J. Appl. Microbiol. 101 (3), 514–525. https://doi.org/10.1111/jam.2006.101.issue-310.1111/j.1365-2672.2005.02736.x.

Setlow, P., 1995. Mechanisms for the prevention of damage to DNA in spores of Bacillus species. Annu. Rev. Microbiol. 49 (1), 29–54. https://doi.org/10.1146/micro.1995.49.issue-110.1146/annurev.mi.49.100195.000333.

Setlow, P., 1988. Small, acid-soluble spore proteins of Bacillus species: structure, synthesis, genetics, function, and degradation. Annu. Rev. Microbiol. 42 (1), 319–338. https://doi.org/10.1146/annurev.mi.42.100188.001535.

Spreter, T., Yip, C.K., Sanowar, S., André, I., Kimbrough, T.G., Vuckovic, M., Pfuetzner, R.A., Deng, W., Yu, A.C., Finlay, B.B., Baker, D., Miller, S.I., Strynadka, N.C.J., 2009. A conserved structural motif mediates formation of the periplasmic rings in the type III secretion system. Nat. Struct. Mol. Biol. 16 (5), 468–476. https://doi.org/10.1038/nsmb.1603.

Steil, L., Serrano, M., Henriques, A.O., Völker, U., 2005. Genome-wide analysis of temporally regulated and compartment-specific gene expression in sporulating cells of Bacillus subtilis. Microbiol. Read. Engl. 151, 399–420. https://doi.org/10.1099/mic.0.27493-0.

Tan, I.S., Ramamurthi, K.S., 2014. Spore formation in Bacillus subtilis. Environ. Microbiol. Rep. 6 (3), 212–225. https://doi.org/10.1111/1758-2229.12130.

Terwilliger, T.C., Grosse-Kunstleve, R.W., Afonine, P.V., Moriarty, N.W., Zwart, P.H., Hung, L.-W., Read, R.J., Adams, P.D., 2008. Iterative model building, structure refinement and density modification with the PHENIX AutoBuild wizard. Acta Crystallogr. D Biol. Crystallogr. 64 (1), 61–69. https://doi.org/10.1107/S090744490705024X.

Thorn, A., Sheldrick, G.M., 2013. Extending molecular-replacement solutions with SHELXE. Acta Crystallogr. D Biol. Crystallogr. 69 (11), 2251–2256. https://doi.org/10.1107/S0907444913027534.

Tosi, T., Estrozi, L.F., Job, V., Guilvout, I., Pugsley, A.P., Schoehn, G., Dessen, A., 2014. Structural similarity of secretins from type II and type III secretion systems. Struct. Lond. Engl. 1993 (22), 1348–1355. https://doi.org/10.1016/j.str.2014.07.005.

Traag, B.A., Pugliese, A., Eisen, J.A., Losick, R., 2013. Gene conservation among endospore-forming bacteria reveals additional sporulation genes in Bacillus subtilis. J. Bacteriol. 195 (2), 253–260. https://doi.org/10.1128/JB.01778-12.

Trouve, J., Mohamed, A., Leisico, F., Contreras-Martel, C., Liu, B., Mas, C., Rudner, D.Z., Rodrigues, C.D.A., Morlot, C., 2018. Structural characterization of the sporulation protein GerM from Bacillus subtilis. J. Struct. Biol. 204 (3), 481–490. https://doi.org/10.1016/j.jsb.2018.09.010.

Uehara, T., Parzych, K.R., Dinh, T., Bernhardt, T.G., 2010. Daughter cell separation is controlled by cytokinetic ring-activated cell wall hydrolysis. EMBO J. 29 (8), 1412–1422. https://doi.org/10.1038/emboj.2010.36.

Worrall, L.J., Hong, C., Vuckovic, M., Deng, W., Bergeron, J.R.C., Majewski, D.D., Huang, R.K., Spreter, T., Finlay, B.B., Yu, Z., Strynadka, N.C.J., 2016. Near-atomic-resolution cryo-EM analysis of the Salmonella T3S injectisome basal body. Nature Adv. 540 (7634), 597–601. https://doi.org/10.1038/nature20576.

Yan, Z., Yin, M., Xu, D., Zhu, Y., Li, X., 2017. Structural insights into the secretin translocation channel in the type II secretion system. Nat. Struct. Mol. Biol. 24 (2), 177–183. https://doi.org/10.1038/nsmb.3350.

Yip, C.K., Kimbrough, T.G., Felise, H.B., Vuckovic, M., Thomas, N.A., Pfuetzner, R.A., Frey, E.A., Brett Finlay, B., Miller, S.I., Strynadka, N.C.J., 2005. Structural characterization of the molecular platform for type III secretion system assembly. Nature 435 (7042), 702–707. https://doi.org/10.1038/nature03554.

Youngman, P.J., Perkins, J.B., Losick, R., 1983. Genetic transposition and insertional mutagenesis in Bacillus subtilis with Streptococcus faecalis transposon Tn917. Proc. Natl. Acad. Sci. 80 (8), 2305–2309.

Zeytuni, N., Flanagan, K.A., Worrall, L.J., Massoni, S.C., Camp, A.H., Strynadka, N.C.J., 2018. Structural and biochemical characterization of SpoIIIAF, a component of a sporulation-essential channel in Bacillus subtilis. J. Struct. Biol. 204 (1), 1–8. https://doi.org/10.1016/j.jsb.2018.06.002.

Zeytuni, N., Hong, C., Flanagan, K.A., Worrall, L.J., Theiltges, K.A., Vuckovic, M., Huang, R.K., Massoni, S.C., Camp, A.H., Yu, Z., Strynadka, N.C., 2017. Near-atomic resolution cryoelectron microscopy structure of the 30-fold homooligomeric SpoIIIAG channel essential to spore formation in Bacillus subtilis. Proc. Natl. Acad. Sci. U. S. A. 114 (34), E7073–E7081. https://doi.org/10.1073/pnas.1704310114.

Zeytuni, N., Strynadka, N.C.J., 2019. A Hybrid Secretion System Facilitates Bacterial Sporulation: A Structural Perspective. Microbiol. Spectr. 7 (1) https://doi.org/10.1128/microbiolspec.PSIB-0013-2018.

Zheng, L., Abhyankar, W., Ouwerling, N., Dekker, H.L., van Veen, H., van der Wel, N.N., Roseboom, W., de Koning, L.J., Brul, S., de Koster, C.G., 2016. Bacillus subtilis Spore Inner Membrane Proteome. J. Proteome Res. 15 (2), 585–594. https://doi.org/10.1021/acs.jproteome.5b00976.

Zimmermann, L., Stephens, A., Nam, S.-Z., Rau, D., Kübler, J., Lozajic, M., Gabler, F., Söding, J., Lupas, A.N., Alva, V., 2018. A Completely Reimplemented MPI Bioinformatics Toolkit with a New HHpred Server at its Core. J. Mol. Biol. 430 (15), 2237–2243. https://doi.org/10.1016/j.jmb.2017.12.007.